Physics of Plasmas ARTICLE scitation.org/journal/php

Observation and analysis of a large banana orbit in the diocotron mode of a coaxial Malmberg–Penning trap

Cite as: Phys. Plasmas **29**, 082103 (2022); doi: 10.1063/5.0098959
Submitted: 13 May 2022 · Accepted: 8 July 2022 ·
Published Online: 2 August 2022

D. L. Eggleston[a)]

AFFILIATIONS

Physics Department, Occidental College, Los Angeles, California 90041, USA

[a)]Author to whom correspondence should be addressed: dleggles@oxy.edu

ABSTRACT

The diocotron mode of an off-axis electron column is studied in a coaxial version of the Malmberg–Penning trap. Measurements of the diocotron frequency as a function of the bias on the central conductor agree well with a derived theory including finite-length corrections and confinement potential contributions. When the experimental parameters are adjusted to give a very low diocotron frequency, the column motion abruptly changes from an axis-encircling orbit to a large banana-shaped orbit in the $r-\theta$ plane with extent $\Delta\theta \approx 270^\circ$ and $\Delta r/R \approx 0.25$, where R is the wall radius. This banana motion is apparently in response to a previously unknown background construction asymmetry. The size of the asymmetric potential is deduced from orbit data and found to be 45–100 mV. Theoretical modeling shows this to be consistent with a small radial offset δ in the center wire position of $\delta/R = 0.034$. Implications and applications of these findings are discussed and a note on obtaining the line density of an electron column in a coaxial trap is given.

I. INTRODUCTION

The Malmberg–Penning trap is a common device for the confinement and study of non-neutral plasmas.[1] It consists of a conducting cylinder divided axially into at least three parts and immersed in a uniform axial magnetic field, **B**. Potentials on the end cylinders provide axial confinement and the axial magnetic field provides radial confinement. The Occidental College trap modifies this basic design by adding a conducting wire running axially down the center of the trap, thus producing a coaxial configuration.[2] The original intention of this modification was to provide a way to adjust the radial electric field (and, thus, the azimuthal $E \times B$ drift) so as to investigate resonances in transport experiments. For these experiments, electrons injected from an off-axis gun were smeared into a low density annular configuration[3] which was then perturbed with applied asymmetric electric fields to produce transport.[4,5] In contrast, this paper reports on experiments where the injected off-axis electron column is left intact and executes azimuthal $E \times B$ motion around the central wire, which we will refer to as the diocotron mode.[6] The electric field producing this motion is set not only by the bias on the center wire but also by the image charges on the trap conductors and by the confining potentials at the ends of the trap. Our experimental measurements of the experimental frequency of this diocotron mode as a function of the center wire bias show good agreement with a theory developed to include these contributions.

When the center wire bias is adjusted so that the sum of these contributions approaches zero, we expect to obtain a stationary column. Instead, we observe that the column orbits cease to be purely azimuthal and instead follow a banana-shaped path in the $r-\theta$ plane, revealing a previously unknown asymmetry in the trap fields.[11] Analysis of these data suggests that this may be due to a small radial offset in the position of the central wire. Although field asymmetries due to construction imperfections have previously been invoked to explain the confinement properties of Malmberg–Penning traps,[12] this result is the most direct measurement of such an asymmetry to date.

The paper is organized as follows: Sec. II gives a brief description of the experimental device. Section III gives experimental results on the diocotron mode in the coaxial trap. Section IV presents the observations of banana orbits which are then analyzed in Sec. V. These results are discussed in Sec. VI. Supporting theory is presented in Sec. VII followed by conclusions in Sec. VIII. A short note on obtaining the line density of an electron column in a coaxial trap is included in Appendix A.

II. EXPERIMENTAL DEVICE

The device used in these experiments (shown schematically in Fig. 1) consists of eight aligned cylinders (inner radius $R = 1.525$ in., length $= 6.000$ in., and inter-electrode gaps $= 0.050$ in.) immersed in an axial magnetic field ($B = 364$ G for experiments in this paper). The cylinders labeled S1–S5 are divided azimuthally into eight equal sectors, labeled as a–h, while G1–G3 are undivided cylinders. As in other traps, two of the cylinders (use G2 and G3 for this description) are biased negatively to provide axial confinement while the rest are grounded. A conducting wire (radius $a = 0.007$ in.) stretched along the axis of the trap allows for control of the radial electric field. The machine is run in repeating cycles: inject, hold, and dump. To start, the potential on G3 and the center wire is grounded. Electrons are injected from a small, off-axis electron gun, producing a long, thin (radius ≈ 2.5 mm) electron column with density $\sim 10^7$ cm^{-3} and axial temperature $kT = 4$ eV. The potentials on G3 and the center wire are then set to their operating values for the remainder of the cycle. During the hold period, charges induced on some of the sectored cylinders are monitored to provide information on the column motion. At the end of a cycle, the potential on G2 is grounded allowing the electrons to leave the trap and hit the phosphor screen, providing information about the position of the electrons as well as their total charge. Other trap details are given elsewhere.[13] It is sometimes desirable to trap columns of varying length. In this paper, these cases are designated by giving the two cylinders on which the trapping potentials are applied. For example, the case just described is denoted G2–G3. An alternate shorthand gives a rough indication of the column length L by giving the number of cylinders between these two confinement cylinders: the G2–G3 case is then denoted L5 since there are five cylinders between G2 and G3.

III. THE FINITE LENGTH DIOCOTRON MODE IN A COAXIAL TRAP

We start with experiments on the coaxial diocotron mode since this provides the necessary background and context for the observation and analysis of the banana orbits. The diocotron mode is well known in conventional Malmberg–Penning traps and consists of the azimuthal $E \times B$ drift of an off-axis plasma column.[14] The drift velocity is set by the z-averaged electric field at the center of the column and this field has contributions from the image charges on the wall of the device and the confining end potentials.[8] A similar mode occurs in the coaxial trap, but the electric field producing the drift now also has contributions from the center wire bias and image charges on the center wire. Also, since the electrons are injected off-axis, there is no need for external excitation of the diocotron mode. The theory for this mode in our trap is given in Sec. VII A.

The diocotron mode can be observed either by monitoring the variation of image charges on a wall sector[15] or by viewing the phosphor screen images as a function of dump time. Typical oscilloscope traces of four wall sectors of ring S2 are shown in Fig. 2 for an electron column confined between cylinders S4 and G2. The wall sectors are connected directly to an oscilloscope and the cable capacitance together with the scope input impedance acts as an integrator circuit. By varying the center wire bias, one can produce diocotron drifts in either counterclockwise [Fig. 2(a)] or clockwise [Fig. 2(b)] directions. Note, however, that for both of the cases shown the center wire bias is positive, thus demonstrating that the drift direction does not depend on the center wire bias alone. Finally, it has been verified that the potentials on the wall sectors have negligible effect on the mode itself by viewing the phosphor screen images with the sectors either grounded or attached to the oscilloscope; no change was observed.

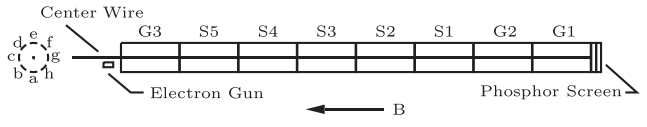

FIG. 1. Schematic of the Occidental College trap. The addition of a conducting center wire produces a coaxial configuration and allows for adjustment of the radial electric field. The five cylinders labeled S1–S5 are divided azimuthally into eight sectors each, labeled as a–h, and shown at the far left as viewed from the gun end of the trap. A narrow electron column is injected from an off-axis gun. Motion of the column is diagnosed by monitoring image charges on the wall sectors or by dumping the column onto a phosphor-coated screen.

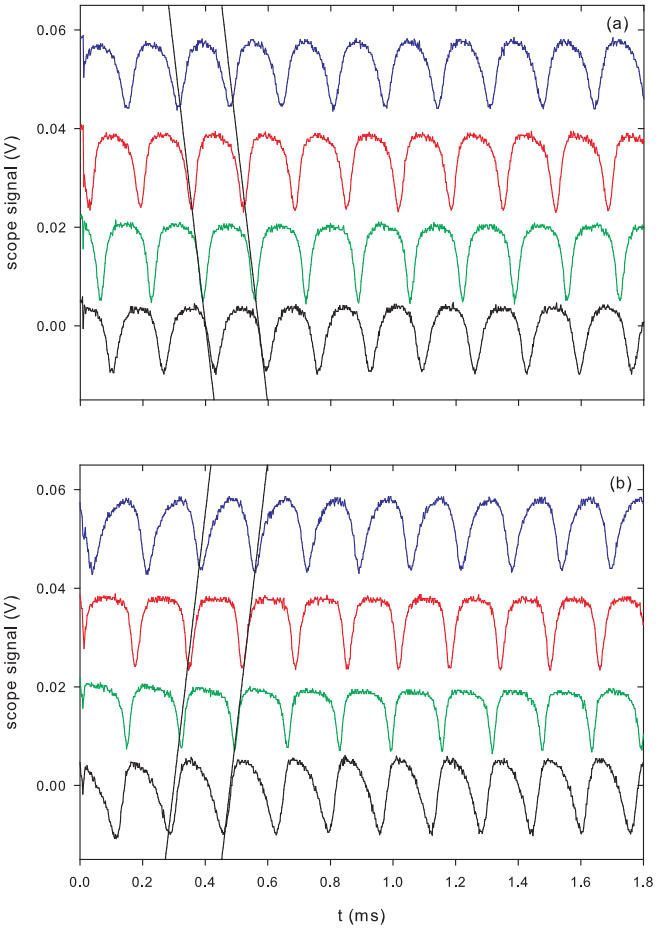

FIG. 2. Wall probe signals arising from a typical diocotron mode. From top to bottom, the signals are from sectors e, c, a, and g of cylinder S2 and the column is trapped between cylinders S4 and G2 (cf. Fig. 1). Signals are offset by 17 mV for clarity and the solid lines are added to show the angular progression of the mode. (a) Counterclockwise rotation observed when the center wire bias is set to 1.60 V. (b) Clockwise rotation observed when the center wire bias is set to 7.36 V.

Figure 3 shows sample data of the variation of the measured diocotron frequency $f_R = v_\theta/2\pi r = -E_r/2\pi rB$ with the center wire bias ϕ_{cw}. Depending on conditions, v_θ (and thus f_R) can be either positive or negative, and the ϕ_{cw} values are chosen to show both cases. Data are shown for two cases: a short column, labeled as L1, with a radius $r/R = 0.56$ and confined between S2 and G2 with a confinement potential of -120 V, and a long column, labeled L5, with a radius $r/R = 0.63$ and confined between G3 and G2 with a confinement potential of -130 V. Both cases show a linear variation of f_R with ϕ_{cw}, although in the L1 case there is a noticeable deviation as f_R approaches zero.

The diocotron frequency depends on the axially averaged radial electric field E_r which includes contributions from the center wire, image charges, and the confining potentials. These are derived in Sec. VII A. An examination of Eqs. (29) and (30) shows that the slope of the f_R vs ϕ_{cw} curves in Fig. 3 is given by $[2\pi r^2 B \ln(a/R)]^{-1}$. Fitting a line to the data and using this equation gives a value for the radial position r of the column that is in good agreement with the value obtained from the phosphor screen image. Indeed, the simplicity of this measurement and analysis makes it a good alternative for finding r in the absence of a phosphor screen.

Obtaining the theoretical value for the x-intercept ϕ_{cw0} of the line is more complicated. As shown in Eq. (31), there are four terms contributing to ϕ_{cw0}, representing contributions from the image charges, finite-length corrections, and the confining potentials. Nevertheless, the resultant calculation (shown by the open symbols in Fig. 3 with the error bars reflecting uncertainty in r and λ, the column line charge density) shows good agreement with the experiment. The contribution of each term in Eq. (31) (including the minus signs) is given in Table I, showing the general need to include these in the theoretical model.

IV. OBSERVATION OF BANANA ORBITS

It appears from the data in Fig. 3 that one can adjust the value of the center wire bias ϕ_{cw} to make the diocotron frequency f_R equal to zero (i.e., a stationary column). As one approaches this condition, however, there is an abrupt change in the wall probe signals. This is shown in Fig. 4 for two values of ϕ_{cw} on either side of the expected $f_R = 0$ value. One can extract some information about the motion of the column from an examination of the signals. The smaller (larger) spikes are produced when the column is farther from (closer to) the wall probe. The added solid lines show that the column is reversing direction periodically. The double spikes in the top and bottom signals of Fig. 4(a) merge in Fig. 4(b) showing that the column reaches but no longer passes sectors e and g, so the azimuthal extent of the orbit is smaller.

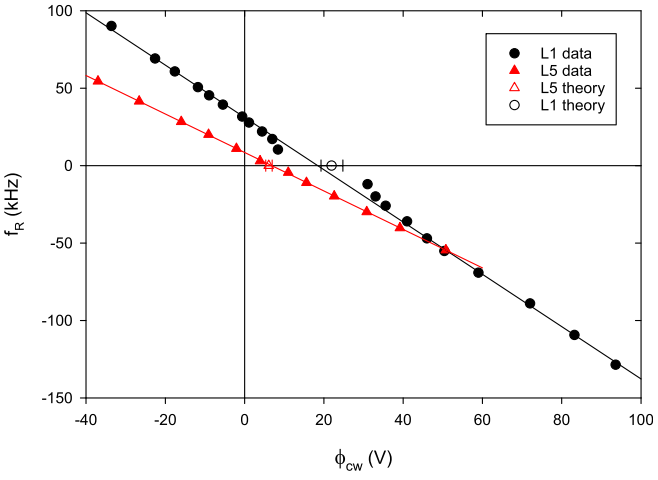

FIG. 3. Sample data showing the variation of diocotron frequency f_R with the center wire bias ϕ_{cw}. The lines are fits to the data. The open symbols are the theoretical values for the x-intercept.

TABLE I. Contributions to the theoretical expressions for ϕ_{cw0} given by Eq. (31) for the data of Fig. 3. The four terms represent the contributions of (1) the image charges on the wall and center wire in an infinite-length model, (2) the finite-length corrections, and (3) and (4) the radial electric field from the confining end potentials.

Term→	1	2	3	4	Total
L5	3.142	−0.069	1.689	1.326	6.088
L1	3.426	−0.530	13.507	5.517	21.920

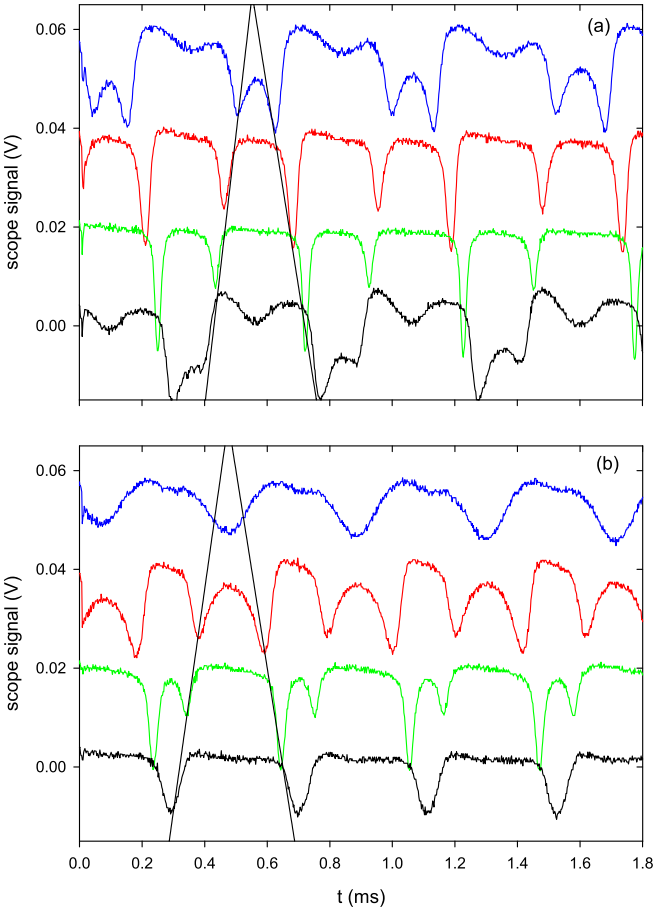

FIG. 4. Wall probe signals showing banana orbits. Solid lines are added to show the reversal of the direction of angular progression. Conditions are the same as for Fig. 2 except for the center wire bias. (a) Center wire bias is set to 6.81 V. (b) Center wire bias is set to 4.37 V.

These conclusions are confirmed and extended by viewing the column motion via the phosphor screen diagnostic. An image is taken using a video camera and frame grabber and the resulting image is analyzed to give the $r-\theta$ coordinates of the column. This is repeated at increasing dump times to show the orbit of the column. The initial position of the column is obtained by dumping the column immediately after capture. Results are displayed in Fig. 5 as viewed from the phosphor screen end of the machine. Notable are the large radial excursion of the orbit ($\Delta r/R \approx 0.25$) and the large θ variation ($\Delta\theta \approx 270°$). For reference, comparing with Fig. 1, sector a is centered at $-90°$, b at $-45°$, c at $0°$, and so on.

Other significant features of the banana orbits are shown in Figs. 6 and 7. In Fig. 6, the initial position of the column is varied using a movable electron gun to show that the banana orbit is bounded by passing orbits at larger and smaller radii. The legend shows the initial r/R value and the initial position is indicated by an open symbol. Data are taken at 10 μs intervals. The arrows show the direction of the orbits above and below the banana and for the banana orbit time increases in the counterclockwise direction. For the $r/R = 0.42$ case, data are taken for two cycles around the screen to better show the orbit.

Figure 7 shows that the radial location of the banana orbit can be varied by adjusting the center wire bias ϕ_{cw}. For these data, the initial radial position of the column is set and then ϕ_{cw} is adjusted to produce a banana orbit at that radius. The legend in the figure shows the initial r/R value and corresponding ϕ_{cw}. The ϕ_{cw} values are found to match, within experimental error, those given by Eq. (31) showing that the banana orbits occur where $\bar{E}_r = 0$. For the cases shown in Fig. 7, $\Delta r/R$ is roughly 0.25 and the period T of the orbits roughly 300 μs.

The banana orbits are apparently produced by the presence of an asymmetric (i.e., θ-dependent) potential. A simple model of the banana oscillations allows one to estimate the size of this potential. The variation in radial position of the column is taken as $r_0 = \bar{r} + \frac{\Delta r}{2}\cos\omega_T t$, where $\omega_T = 2\pi/T$ is the oscillation frequency. The maximum value of the radial velocity $v_r = dr/dt$ is then $v_r^{\max} = \omega_T \Delta r/2$. Taking the z-averaged asymmetric potential to have the form $\bar{\psi}(r)\cos l\theta$, the maximum value of the radial $E\times B$ drift is $v_r^{\max} = E_\theta^{\max}/B = l\bar{\psi}(\bar{r})/\bar{r}B$. Equating these gives $\bar{\psi}(\bar{r}) = \pi\bar{r}B\Delta r/lT$. Values for $\bar{\psi}$ obtained for the four cases of Fig. 7 are given in Table II, where the rightmost limit of the orbits has been used for $\bar{r}$ and we have taken $l = 1$.

While the focus in this paper is on the initial behavior of the column motion, we have made some observations of the long-term evolution. The diocotron orbits are essentially undamped on short time scales, but the wall signals decrease in amplitude over the same timescale (~100 ms) as the loss of particles, i.e., the transport timescale. For the banana orbits, the transport timescale is shorter (~20–40 ms). On this timescale, we have observed cases where a banana orbit becomes a passing orbit and cases where the radial and azimuthal extents of the banana orbit gradually shrink until the column is either left stationary at or executes small oscillations around $\theta \approx -70°$. While we do not yet fully understand these behaviors, it seems reasonable that the orbit should change on the timescale for particle loss since the asymmetry amplitude depends on the column's line charge [see Eq. (38)].

We have made some attempt to cancel the asymmetry producing the banana orbit by applying potentials to various wall sectors in the confinement region. While such applied potentials do affect the banana orbit, changing its radial position and/or its orientation, we have been unable to obtain a configuration that eliminates the banana orbit altogether.

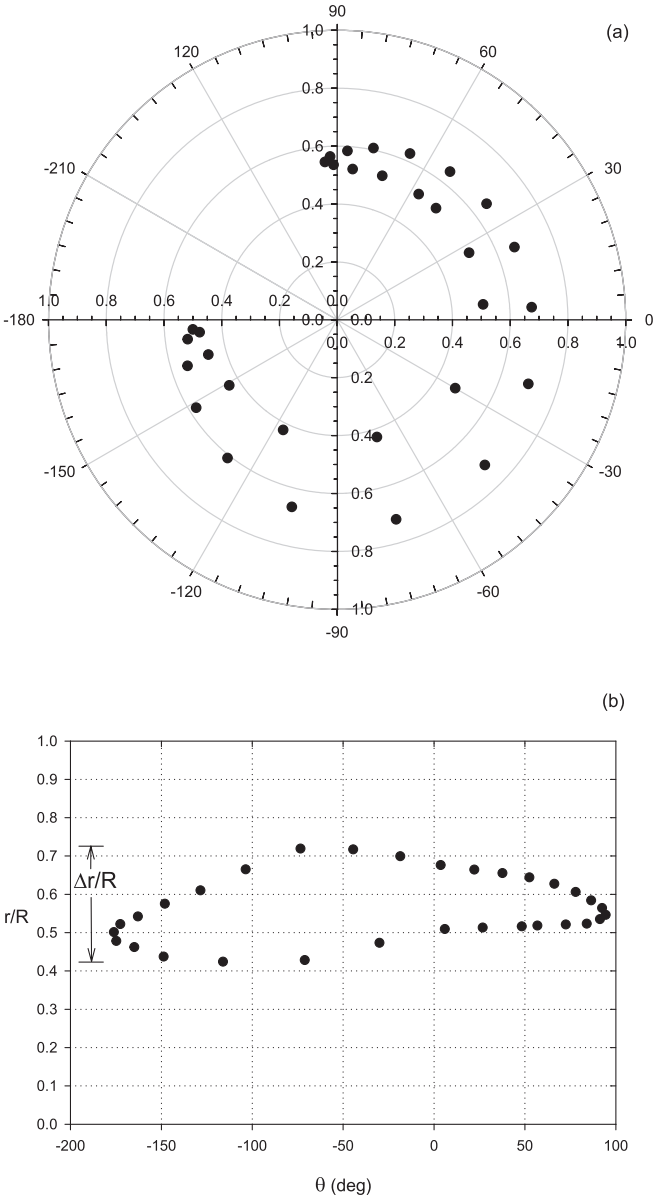

FIG. 5. Coordinates of the column (r/R and θ) extracted from phosphor screen images showing a banana orbit for G2–G3 trap and $\phi_{cw} = 5.16$ V. The initial position is $r/R = 0.52$ and $\theta = 57°$ and the time between points is 10 μs. (a) Data as seen from the phosphor screen end of the machine displayed in a polar plot to define the coordinate system. The angular range is taken as $-210°$ to $150°$ to accommodate the orientation of the banana orbit. For reference, comparing with Fig. 1, sector a is centered at $-90°$, b at $-45°$, c at $0°$, and so on. (b) Same data displayed in a scatterplot. The definition of the full banana width $\Delta r/R$ is indicated.

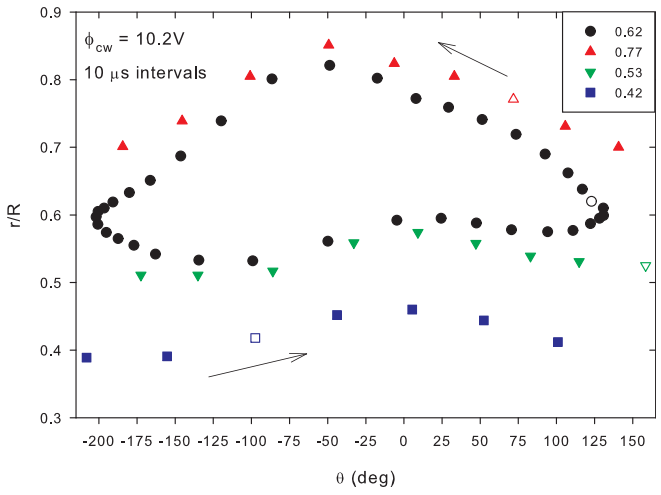

FIG. 6. Orbits produced with differing initial radius values for a fixed center wire bias showing that the banana orbit is bounded by passing orbits. G2–G3 trap and $\phi_{cw} = 10.2$ V. The legend shows the initial r/R which is also indicated by the open symbol for each series. The time between points is 10 μs.

V. ANALYSIS

To investigate the axial dependence of the asymmetry, the experiment has been run with a short L1 electron column trapped at various axial positions in the trap (i.e., G3–S4, S5–S3, etc.). The banana orbit is observed at each location and shows little variation. I conclude that the asymmetry producing the banana orbit has little or no axial variation.

The particular orientation of the banana orbit (roughly symmetrical around $\theta \approx -40^\circ \equiv \theta_w$ in Fig. 5) led to an examination of the trap construction for any element with that orientation. It was found

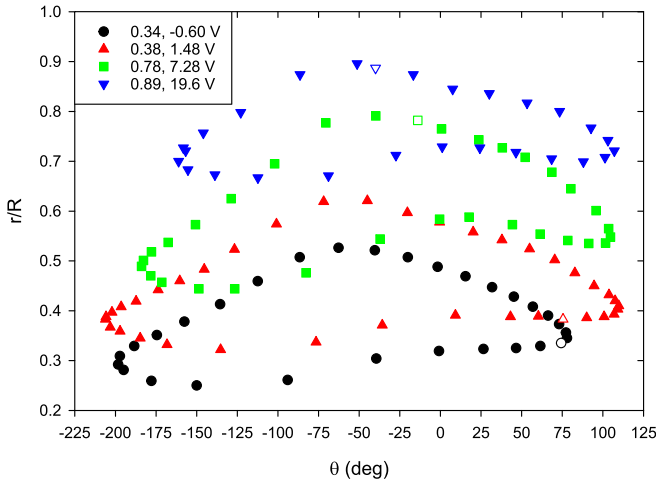

FIG. 7. The banana orbit changes its radial position as the center wire bias is varied. Examples from a G2–G3 trap. The legend shows initial r/R and ϕ_{cw} values. Initial position is also indicated by the open symbol for each plot. Time between points is 10 μs and time increases in the counterclockwise direction.

TABLE II. Experimental values of $\bar{r}/R$, ϕ_{cw}, and $\bar{\psi}$ for the four cases of Fig. 7. The rightmost limit of the orbits has been used for $\bar{r}$.

$\bar{r}/R$	0.345	0.410	0.548	0.721
ϕ_{cw}(V)	−0.60	1.48	7.28	19.6
$\bar{\psi}$(mV)	45.6	52.1	79.8	100.4

that the center wire support at the screen end of the trap has that orientation and this led to the hypothesis that the asymmetry is produced by the center wire not being exactly on-axis. Since care was taken during the assembly of the trap to ensure proper positioning of the wire, it is hard to believe that it could be offset by much from a central position. So the question arises, how much offset would it take to produce an asymmetry of the size observed?

To obtain an estimate of the offset, the following calculation is performed. It is convenient to place the wire centered at $r = 0$ and let the grounded wall be offset by some small amount δ in the direction θ_w. The (r, θ) coordinates of the wall are then related by $r = \delta\cos\tilde{\theta} + \sqrt{R^2 - \delta^2 + (\delta\cos\tilde{\theta})^2} \approx R + \delta\cos\tilde{\theta}$, where $\tilde{\theta} = \theta - \theta_w$ and the approximation is good to first order in the small parameter δ/R. This configuration is approximately equivalent to a centered wall of radius R having a non-zero potential that varies as $-\delta d\phi/dr\cos\tilde{\theta}$, where ϕ is the potential at the wall calculated without an offset. Laplace's equation can then be solved subject to these boundary conditions giving the theoretical value of the asymmetric potential produced by the offset. Since one can measure the amplitude of this potential, it is then possible to use this experimental value in the theoretical expressions to find the implied offset. The necessary theoretical expression is obtained in Sec. VII B. The results for the four cases of Fig. 7 are included in Table III. Note the consistency of the δ/R values for the four cases, with the standard deviation being about 9% of the average. This consistency supports the validity of the model. Using the average value $\delta/R = -0.0343$ and the measured R gives $\delta = -0.052$ inches $= -1.3$ mm, a plausible value although distressingly large given the care that was taken in the construction of the trap. The negative sign means that the direction of the offset is opposite to the assumed direction of -40°. Note that the small size of δ/R is consistent with the assumptions of the model. This offset is large compared to the estimated gravitational sag in the wire of 0.0028 in. = 0.071 mm

TABLE III. Calculated values for the five terms in the curly bracket of Eq. (38) and the resulting value for δ/R using the experimental parameters of the four cases of Fig. 7. The corresponding experimental ϕ_{cw} and $\bar{\psi}$ values are given in Table II. The five terms represent the relative contributions of (1) the center wire potential, (2) the electron column and its image charges in an infinite-length model, (3) the finite-length corrections to this model, and (4) and (5) the confining potentials.

$\bar{r}/R$	Term →	1	2	3	4	5	δ/R
0.345		−0.038	−0.640	0.019	−0.400	−0.271	−0.034
0.410		0.113	−0.912	0.025	−0.460	−0.320	−0.034
0.548		0.741	−1.815	0.044	−0.599	−0.447	−0.039
0.721		2.625	−4.404	0.081	−0.853	−0.717	−0.031

VI. DISCUSSION

Several comments on these results are in order. The discovery of the asymmetry was made only because the coaxial configuration allows for the attainment of the $f_R \approx 0$ condition by adjusting ϕ_{cw}. At ϕ_{cw} values far from this condition (as have commonly been used in the transport experiments on this device), the effect of the asymmetry would be too small to be directly observed. This shows an advantage of the coaxial configuration for detecting small asymmetric fields.

If the asymmetry is indeed caused by an offset center wire, future versions of coaxial traps might include an adjustment of the wire's end supports so that any offset can be minimized. On the other hand, a deliberate offset of the center wire producing an asymmetric potential could be used to adjust the radial position of the column. This can be seen from the data shown in Fig. 7. A column starting at $r/R = 0.89$ with $\phi_{cw} = 19.6$ V could be allowed to evolve until the orbit crossed the $\phi_{cw} = 7.28$ V curve, at which point the center wire bias would be switched to that value. The column would then be allowed to evolve until it crossed the $\phi_{cw} = 1.48$ V curve where the center wire would again be switched. Repeating the process (or some suitable variation of it) would allow one to position the column at practically any radius.

We have made a preliminary test of this position manipulation technique, switching ϕ_{cw} to a new value at the innermost point in the banana orbit. When the new ϕ_{cw} value was selected appropriately, the column orbit did indeed shift to a banana at a smaller radius. Repeating this process twice, we caused the inner edge of the banana orbit to move from $r/R = 0.51$ to 0.30.

The possible effect of this asymmetry on previous transport experiments should be noted. In those experiments,[4,5] the injected electrons are first smeared into a low-density annulus. Then, an applied asymmetry, produced by voltages applied to the sectors of the confinement region, is used to produce radial transport. Since the density is low, the applied asymmetry is essentially the vacuum field, which can be readily calculated. Both the fields and the resulting experimental transport are then known, allowing for close comparisons between experiment and theory. This paper has shown that there is another asymmetry, likely produced by an offset center wire, which has not been previously accounted for. While the amplitudes of this asymmetry shown in Table II are less than those applied in the transport experiments (typically a few tenths of a volt), this comparison is misleading because the conditions in the transport experiments are not the same as those in this paper. Referring to Eq. (38), the second through fourth terms are proportional to λ_0 and will decrease when the electron column is smeared out. The fifth term, depending on the electron temperature, would not change significantly. The value of ϕ_{cw} used in the transport experiments, however, is significantly larger (typically ~ -80 V), so the first term would dominate and the value of $\bar{\psi}$ could be comparable to that of the applied asymmetry. The presence of $\bar{\psi}$ would, thus, need to be accounted for in any future comparison between experiment and theory, but this is beyond the scope of this paper.

VII. SUPPORTING THEORY

In this section, we derive the results referred to in Secs. III–VI. First, we derive the axially integrated radial electric field that sets the diocotron frequency. Then, we use these results to calculate the amount of radial offset in the center wire position needed to produce a given asymmetry amplitude.

A. The finite length diocotron mode in a coaxial trap

The azimuthal $\mathbf{E} \times \mathbf{B}$ drift of an off-axis electron column in a coaxial trap is produced by an electric field having contributions from three sources: (1) the biased center wire, (2) the image charges on the conducting wall and center wire, and (3) the radial component of the confining fields at the ends of the trap. In this section, each of these contributions is calculated. I follow the method of Fine and Driscoll[8] but give details, since this is the first time (to my knowledge) these methods have been applied to a coaxial trap and in this context a number of complications arise.

Taking the three contributions in order, the potential due to an infinitely long biased center wire (potential ϕ_{cw}, radius a) bounded by a grounded cylinder at radius R is easily found by direct integration of Laplace's equation. The result is

$$\phi(r) = \phi_{cw} \frac{\ln(r/R)}{\ln(a/R)}. \tag{1}$$

To determine the contribution of the image charges, we must solve Poisson's equation for an arbitrary charge distribution $\rho(\mathbf{r})$

$$\nabla^2 \phi(\mathbf{r}) = -\rho(\mathbf{r})/\epsilon_0. \tag{2}$$

To allow $\rho(\mathbf{r})$ to have finite length, the Green's function method is employed. In this method, Green's function $G(\mathbf{r}, \mathbf{r}')$ is first found by solving

$$\nabla^2 G(\mathbf{r}, \mathbf{r}') = \delta^3(\mathbf{r} - \mathbf{r}') \tag{3}$$

and the result is then used to obtain the potential

$$\phi(\mathbf{r}) = -\frac{1}{\epsilon_0} \int dV' G(\mathbf{r}, \mathbf{r}') \rho(\mathbf{r}'). \tag{4}$$

Here, $\mathbf{r}$ and $\mathbf{r}'$ are the field and source position vectors, respectively; δ^3 is the three-dimensional delta function; dV' is a volume element; and the integral is over a volume including all the sources. The correctness of this method can be seen by applying the Laplacian operator to Eq. (4). Applying Eq. (3) then gives Eq. (2) which shows that Eq. (4) is indeed the solution to Eq. (2).

For this problem, the Laplacian and δ^3 are written in cylindrical coordinates (r, θ, z)

$$\frac{1}{r}\frac{\partial}{\partial r}\left(r\frac{\partial G}{\partial r}\right) + \frac{1}{r^2}\frac{\partial^2 G}{\partial \theta^2} + \frac{\partial^2 G}{\partial z^2} = \frac{1}{r}\delta(r - r')\delta(\theta - \theta')\delta(z - z'). \tag{5}$$

Next, the Fourier transform and series[16] are used

$$\delta(z - z') = \frac{1}{2\pi} \int_{-\infty}^{\infty} dk e^{ik(z-z')} \tag{6}$$

and

$$\delta(\theta - \theta') = \frac{1}{2\pi} \sum_{m=-\infty}^{\infty} e^{im(\theta-\theta')} \tag{7}$$

and we assume that G can be written as

$$G(\mathbf{r}, \mathbf{r}') = \frac{1}{4\pi^2} \sum_{m=-\infty}^{\infty} \int_{-\infty}^{\infty} dk\, g_m(k, r, r') e^{im(\theta-\theta')} e^{ik(z-z')}. \tag{8}$$

Using these in Eq. (5), the differential equation for $g_m(k, r, r')$ is obtained

$$\frac{1}{r}\frac{d}{dr}\left(r\frac{dg_m}{dr}\right)-\left(k^2+\frac{m^2}{r^2}\right)g_m=\frac{1}{r}\delta(r-r'). \tag{9}$$

The solutions to Eq. (9) for $r \neq r'$ are the modified Bessel functions $I_m(kr)$ and $K_m(kr)$,[17] so, generally, g_m will be a combination of these with coefficients that allow the various boundary conditions to be satisfied. Rather than immediately focusing on the current problem, a general approach applicable to a variety of cases is developed.

Let $\xi_1(kr)$ be a linear combination of the modified Bessel functions for $r < r'$ and $\xi_2(kr)$ be an independent linear combination for $r > r'$. Assume that $\xi_1(kr)$ and $\xi_2(kr)$ have been constructed to satisfy whatever boundary conditions are present for $r < r'$ and $r > r'$, respectively. Then, we take

$$\begin{aligned} g_m(k,r,r') &= C_1(r')\xi_1(kr) \quad (r<r') \\ &= C_2(r')\xi_2(kr) \quad (r>r'), \end{aligned} \tag{10}$$

where C_1 and C_2 are to be determined by applying the continuity and jump conditions at $r = r'$. The first of these gives

$$C_1(r')\xi_1(kr') = C_2(r')\xi_2(kr'). \tag{11}$$

The jump condition is obtained by integrating Eq. (9) from $r' - \epsilon$ to $r' + \epsilon$, giving

$$\left[r\frac{dg_m}{dr}\right]_{r'-\epsilon}^{r'+\epsilon}=1. \tag{12}$$

Letting $\epsilon \to 0$, one obtains

$$C_2(r')\xi_2'(kr') - C_1(r')\xi_1'(kr') = 1/r', \tag{13}$$

where $\xi_1' = d\xi_1/dr$ and $\xi_2' = d\xi_2/dr$.

To complete the determination of C_1 and C_2, a useful result involving the Wronskian $W = \xi_1\xi_2' - \xi_2\xi_1'$ is employed. Taking the derivative of W with respect to r, one obtains $W' = \xi_1'\xi_2' + \xi_1\xi_2'' - \xi_2'\xi_1' - \xi_2\xi_1''$. Since ξ_1 and ξ_2 satisfy Eq. (9), one can use that equation to obtain ξ_1'' and ξ_2''. After some cancelation, one obtains $W' = -W/r$, which can be integrated to obtain

$$W = \xi_1(kr')\xi_2'(kr') - \xi_2(kr')\xi_1'(kr') = A/r', \tag{14}$$

where A is an integration constant to be determined and the result has been evaluated at $r = r'$. One can now solve Eqs. (11), (13), and (14) to find $C_1(r') = \xi_2(kr')/A$ and $C_2(r') = \xi_1(kr')/A$. Equation (10) then becomes

$$\begin{aligned} g_m(k,r,r') &= \xi_2(kr')\xi_1(kr)/A \quad (r<r') \\ &= \xi_1(kr')\xi_2(kr)/A \quad (r>r'), \end{aligned} \tag{15}$$

which can be written in the compact form as

$$g_m(r,r') = \xi_1(kr_<)\xi_2(kr_>)/A, \tag{16}$$

where $r_<$ ($r_>$) is the smaller (larger) of r and r'.

The constant A is determined from Eq. (14) using the ξ_1 and ξ_2 forms appropriate for the boundary conditions of the problem. As an example, consider a charge distribution in space with no conducting boundaries.[19] Our boundary requirements are that ξ_1 and ξ_2 are finite at $r = 0$ and $r = \infty$, respectively, so, given the behavior of the Bessel functions at these limits,[17] $\xi_1(kr) = I_m(kr)$ and $\xi_2(kr) = K_m(kr)$ are satisfactory choices. Using these in Eq. (14) and employing the properties of the Bessel functions,[17] the simple result $A = -1$ is obtained and

$$g_m(k,r,r') = -I_m(kr_<)K_m(kr_>). \tag{17}$$

For the coaxial trap, the boundary conditions are $\phi = 0$ at $r = a$ and $r = R$, so appropriate choices are $\xi_1(kr) = I_m(kr)K_m(ka) - I_m(ka)K_m(kr)$ and $\xi_2(kr) = I_m(kr)K_m(kR) - I_m(kR)K_m(kr)$ which then give $A = K_m(ka)I_m(kR) - K_m(kR)I_m(ka)$. Note that the potential due to a non-zero bias on the center wire is known and can be added in later. The result is

$$g_m(k,r,r') = \frac{[I_m(kr_<)K_m(ka) - I_m(ka)K_m(kr_<)][I_m(kr_>)K_m(kR) - I_m(kR)K_m(kr_>)]}{K_m(ka)I_m(kR) - K_m(kR)I_m(ka)}. \tag{18}$$

To obtain the potential using Eq. (4), the charge distribution $\rho(\mathbf{r}')$ must be specified. For this experiment where the column radius is small compared to R, the electron column can reasonably be modeled as a line charge extending in the $z-$direction and centered at (r_0, θ_0)

$$\rho(\mathbf{r}') = \frac{\lambda(z')}{r'}\delta(r'-r_0)\delta(\theta'-\theta_0). \tag{19}$$

Using this in Eq. (4) gives

$$\phi(\mathbf{r}) = -\frac{1}{4\pi^2\epsilon_0}\sum_{m=-\infty}^{\infty}\int_{-\infty}^{\infty}dk\int_{-\infty}^{\infty}dz'\,\lambda(z')e^{im(\theta-\theta_0)}e^{ik(z-z')}g_m(k,r,r_0). \tag{20}$$

It is useful to note that, in the case of an infinite-length column [i.e., $\lambda(z') = \lambda_0$ constant], the z' integral can be performed using the following relation:

$$\int_{-\infty}^{\infty}dz'\,e^{-ikz'} = 2\pi\delta(k). \tag{21}$$

Then, in performing the k-integral in Eq. (20), one may replace the Bessel functions in Eq. (18) with their small k limits.[17] This gives

$$\phi(r,\theta) = \frac{\lambda_0}{2\pi\epsilon_0}\left\{\frac{\ln(r_</a)\ln(r_>/R)}{\ln(a/R)} + \sum_{m=1}^{\infty}\frac{\cos m(\theta-\theta_0)}{m\left(1-\left(\frac{a}{R}\right)^{2m}\right)} \times\left[\left(\frac{a^2r_>}{R^2r_<}\right)^m + \left(\frac{r_<}{r_>}\right)^m - \left(\frac{r_>r_<}{R^2}\right)^m - \left(\frac{a^2}{r_>r_<}\right)^m\right]\right\}. \tag{22}$$

The results obtained so far give the potential produced by both the electron column and the image charges in the conducting wall and

center wire. For the calculation of the diocotron frequency, one is interested in finding the potential produced by the image charges alone. The appropriate Green's function, which I call $g_{mi}(k, r, r_0)$, is obtained by subtracting Eq. (17) from Eq. (18). I denote the radial derivative of this as $g'_{mi}(k, r, r_0) = dg_{mi}(k, r, r_0)/dr$.

To proceed, I further specify that the line charge has a constant value λ_0 and extends from $z = -L/2$ to $L/2$. Then, the $z'-$ integral can be evaluated, giving $\frac{2}{k}\sin\left(\frac{kL}{2}\right)$. In the experiment, the axial bounce frequency is large compared to the azimuthal drift frequency, so it makes sense to use the $z-$averaged value of the electric field $\bar{E}_r = \frac{1}{L}\int E_r dz$ where the integral is from $z = -L/2$ to $L/2$. Then, the $z-$ integral can also be evaluated, giving another factor of $\frac{2}{k}\sin\left(\frac{kL}{2}\right)$. The result is (adding the subscript i to denote the image field)

$$\bar{E}_{ri} = \frac{\lambda_0}{4\pi^2\epsilon_0 L}\left[\sum_{m=-\infty}^{\infty}\int_{-\infty}^{\infty} dk\, e^{im(\theta-\theta_0)}\left(\frac{2}{k}\sin\left(\frac{kL}{2}\right)\right)^2 g'_{mi}(k, r, r_0)\right], \tag{23}$$

which will be evaluated at the location of the electron column, $r = r_0$ and $\theta = \theta_0$. Note that the sum over m can be written in terms of real functions as $1 + \sum_{m=1}^{\infty} 2\cos m(\theta - \theta_0)$.

To proceed, the square bracket in Eq. (23) is numerically evaluated using Mathematica.[18] The dimensionless parameters r_0/R and $C \equiv L/2R$ are varied and it is found that, for C greater than some value C_0, the bracket varies linearly with C and is well represented by $A(r_0) + C \times B(r_0)$. The linear threshold value C_0 varies from about 0.3 for r_0/R values of 0.1 or 0.9 to about 0.8 for $r_0/R = 0.5$, so the linear variation with C applies to all but the very shortest columns. The functions $A(r_0)$ and $B(r_0)$ are shown by the closed circles in Fig. 8. The simple form of this result leads one to compare with a calculation of E_{ri} for an infinite-length line charge. This can be obtained from a z-independent solution of Poisson's equation[20] or by using g_{mi} in Eq. (20) and applying the procedure leading to Eq. (22) to obtain the potential produced by the image charges, $\phi_i(r, \theta)$. Then, $E_{ri\infty} = -\partial\phi_i/\partial r$ evaluated at $r = r_0$, $\theta = \theta_0$. The result can be written

$$E_{ri\infty} = -\frac{\lambda_0}{2\pi\epsilon_0 r_0}\left\{\frac{\ln(r_0/R)}{\ln(a/R)} - \sum_{n=1}^{\infty}\left[\frac{(r_0/R)^{2n} - (a/r_0)^{2n}}{1 - (a/R)^{2n}}\right]\right\}$$
$$\equiv -\frac{\lambda_0}{2\pi\epsilon_0 r_0} D(r_0), \tag{24}$$

where $D(r_0)$ is the curly bracket in Eq. (24). This, multiplied by $-4\pi R/r_0$, is plotted as the solid line in Fig. 8(b), showing good agreement. The result of Eq. (23) may, thus, be written as

$$\bar{E}_{ri} = E_{ri\infty} + \frac{\lambda_0}{4\pi^2\epsilon_0 L} A(r_0). \tag{25}$$

Finally, the contribution to the column's azimuthal drift from the radial component of the confining electric field at the ends of the trap is considered. The confining potential was previously found in Ref. 21 and is given by

$$\phi_{end}(r, z_c) = -\sum_{m=0}^{\infty} A_m \tilde{F}_0(k_m r) e^{-k_m z_c}, \tag{26}$$

where $\tilde{F}_0(k_m r) = J_0(k_m r)Y_0(k_m a) - J_0(k_m a)Y_0(k_m r)$, J_0 and Y_0 are Bessel functions of the first and second kind,[17] k_m are the k values satisfying $\tilde{F}_0(kR) = 0$, z_c is measured from the end of the confining cylinder, and A_m is defined in Ref. 21. The potential due to the center wire bias is z-independent and, thus, not relevant to this calculation. For our calculation of the diocotron frequency, one is interested in the radial electric field produced by the confining potential

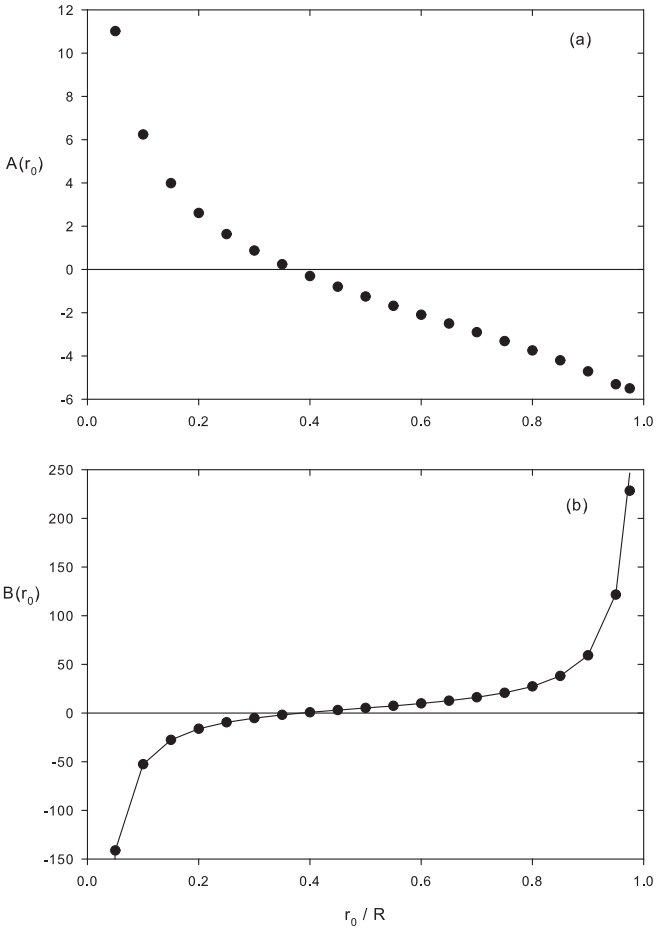

FIG. 8. Plots of the quantities A and B defined in the text vs the scaled column position r_0/R. The closed circles show values obtained numerically. (a) Plot of $A(r_0)$ vs r_0/R. (b) Plot of $B(r_0)$ vs r_0/R. The solid line is the curly bracket in Eq. (24) multiplied by $-4\pi R/r_0$ showing that the quantity B is related to E_{ri} for an infinite-length line charge.

$$E_r(r, z_c) = -\sum_{m=0}^{\infty} A_m k_m \tilde{F}_1(k_m r) e^{-k_m z_c}, \tag{27}$$

where $\tilde{F}_1(k_m r) = J_1(k_m r)Y_0(k_m a) - J_0(k_m a)Y_1(k_m r)$.

As in the calculation of E_{ri}, we are interested in the z-averaged value of E_r. The first step is to find the plasma reflection point z_{cr} using energy conservation by equating the total energy at the axial center of the plasma column ($E_{tot} = kT + q\phi_{col}$, with T being the temperature) with the potential energy at z_{cr} [i.e., $q\phi_{end}(z_{cr})$]. Note that knowing z_{cr} also allows one to determine the column length L. Because ϕ_{end} involves an infinite sum of terms involving z_c, finding z_{cr} must, in general, be done numerically. In practice, however, it is often sufficient to

employ the approximation of keeping just the first term of the sums in Eqs. (26) and (27). Then, the energy conservation step gives $E_{tot} \approx -q\tilde{F}_0(k_0 r)A_0 \exp(-k_0 z_{cr})$. Axially averaging E_r from z_{cr} to $z_{cr} + L/2$ (the middle of the plasma column of length L) then gives

$$\bar{E}_r \approx \frac{2}{L}\tilde{F}_1(k_0 r)[e^{-k_0 L/2} - 1]A_0 e^{-k_0 z_{cr}} \approx \frac{2}{L}\frac{E_{tot}}{q}\tilde{C}(r_0) = \frac{2\tilde{C}(r_0)}{L}\left[\frac{kT}{q} + \frac{\lambda_0}{2\pi\epsilon_0}J(r_0)\right], \tag{28}$$

where $\tilde{C}(r_0) = \tilde{F}_1(k_0 r_0)/\tilde{F}_0(k_0 r_0)$, $J(r_0)$ is the curly bracket in Eq. (22) evaluated at the column location (i.e., $r = r_0$, $\theta = \theta_0$) and, in the second step, the term $\exp(-k_0 L/2)$ is ignored as negligible compared to 1. It is interesting to note that, in this approximation, the confining potential does not appear in the expression for $\bar{E}_r$. While a larger confining potential produces a larger E_r, it also restricts the electrons from penetrating into the confinement rings. The two effects cancel leaving no dependence on confining potential. The confining potential does, however, effect the calculation of $\bar{E}_r$ in the determination of the column length L.

Putting it all together, the total radial electric field producing the diocotron mode is given by

$$\bar{E}_r = E_\infty + \frac{\lambda_0}{4\pi^2\epsilon_0 L}A(r_0) + \frac{2\tilde{C}(r_0)}{L}\left[\frac{kT}{q} + \frac{\lambda_0}{2\pi\epsilon_0}J(r_0)\right], \tag{29}$$

where now including the field produced by the center wire bias ϕ_{cw}

$$E_\infty = -\frac{1}{r_0}\left[\frac{\phi_{cw}}{\ln(a/R)} + \frac{\lambda_0}{2\pi\epsilon_0}D(r_0)\right]. \tag{30}$$

The value of the center wire bias giving $\bar{E}_r = 0$ is then

$$\phi_{cw0} = \ln(R/a)\left\{\frac{\lambda_0}{2\pi\epsilon_0}\left[D(r_0) - \frac{A(r_0)}{2\pi}\frac{r_0}{L} - 2\tilde{C}(r_0)J(r_0)\frac{r_0}{L}\right] - \frac{2\tilde{C}(r_0)kT}{q}\frac{r_0}{L}\right\}. \tag{31}$$

Going from left to right, the first term is due to the image charges on the wall and center wire in an infinite-length model. The second term is due to finite-length corrections, and the third and fourth terms are due to the radial electric field from the confining end potentials. The quantities $\tilde{C}(r_0)$, $D(r_0)$, and $J(r_0)$ are plotted vs the scaled radius r_0/R in Fig. 9 using parameters that match the experimental device.

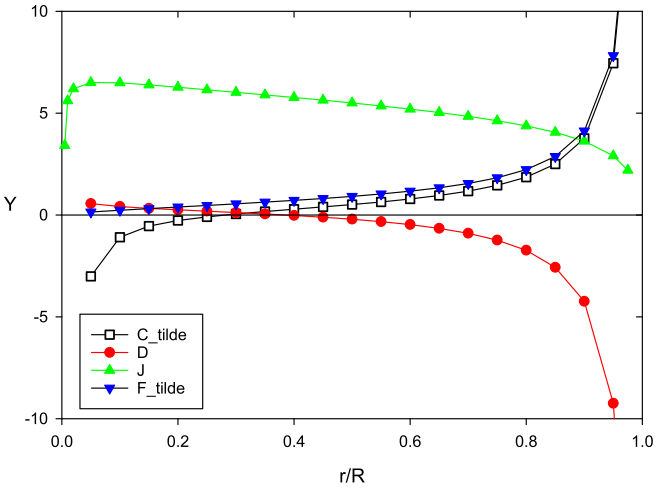

FIG. 9. This figure shows $\tilde{C}$, D, J, and $\tilde{F}$ vs r_0/R. These functions are defined in the text.

B. Potential produced by a radially offset wall

In this section, we calculate the asymmetric potential ψ produced by a wall potential of the form $-\delta d\phi/dr|_R \cos\tilde{\theta}$, where δ is the offset constant and ϕ is the potential found in Sec. VII A. For such a boundary, we generally expect a potential of the form $\psi(r,z)\cos\tilde{\theta}$ and Laplace's equation reduces to $\partial^2\psi/\partial r^2 + \partial\psi/r\partial r - \psi/r^2 + \partial^2\psi/\partial z^2 = 0$. As we have seen in Sec. VII A, the potential ϕ has contributions from the biased center wire, the electron column and its image charges, and the confining fields at the ends of the trap. The center wire potential has no z-dependence so $\partial^2\psi/\partial z^2 = 0$ and Laplace's equation has solutions of the form $\psi(r) = Ar + Br^{-1}$, with A and B constants determined by the boundary conditions $\psi(a) = 0$ (since there is no θ-variation on the center wire) and $\psi(R) = -\delta d\phi/dr|_R$. Using Eq. (1), we obtain

$$\psi(r) = -\frac{\delta}{R}\frac{\phi_{cw}}{\ln(a/R)}\frac{r}{R}\frac{1 - a^2/r^2}{1 - a^2/R^2}. \tag{32}$$

Considering next the contribution from the finite-length electron column and its images, the solution will have the form $\psi(r,z) = \int dk \exp(ikz)[A_k I_1(kr) + B_k K_1(kr)]$, where $I_1(kr)$ and $K_1(kr)$ are modified Bessel functions of first order, A_k and B_k are constants, and the integral is from $-\infty$ to $+\infty$. In this case, we use Eq. (20) to determine the boundary condition at the wall. It should be noted that this boundary condition is dynamic, changing as the column moves, but since we are seeking the maximum amplitude of the asymmetric potential, we set $\theta_0 = \theta_w$. We then proceed as in Sec. VII A, taking the column as a constant line charge of length L. After obtaining $\psi(r,z)$, we find the z-averaged potential and evaluate at the column position, obtaining

$$\bar{\psi}(r_0) = \delta\frac{\lambda_0}{4\pi^2\epsilon_0 L}\left[\int_{-\infty}^{\infty} dk \left(\frac{2}{k}\sin\left(\frac{kL}{2}\right)\right)^2 \gamma(k,R,r_0) \times \frac{I_1(kr_0)K_1(ka) - I_1(ka)K_1(kr_0)}{I_1(kR)K_1(ka) - I_1(ka)K_1(kR)}\right], \tag{33}$$

where $\gamma(k,R,r_0) = g'_0(k,R,r_0) + 2\sum_{m=1}^{\infty} g'_m(k,R,r_0)$. As in Sec. VII A, we numerically evaluate the square bracket and find that it varies linearly with $C = L/2R$ and can be represented by $A_1(r_0) + C \times B_1(r_0)$, with the functions $A_1(r_0)$ and $B_1(r_0)$ shown by the closed circles in Fig. 10. We have verified that $B_1(r_0)$ is related to ψ produced by an infinite-length line charge using Eq. (22) for the boundary condition at $r = R$. Thus, we can write

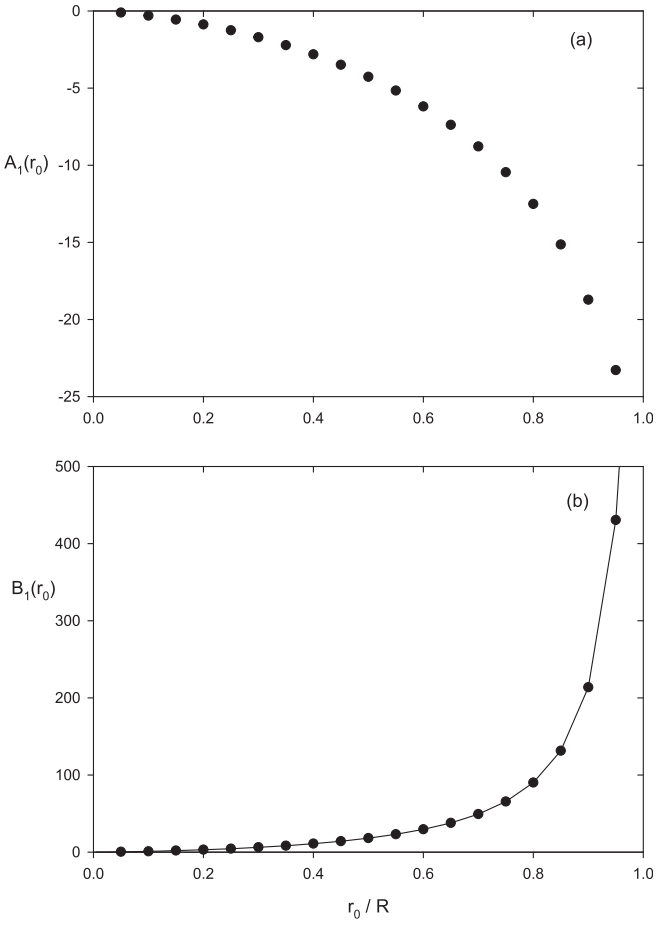

FIG. 10. Plots of the quantities A_1 and B_1 defined in the text vs the scaled column position r_0/R. The closed circles show values obtained numerically. (a) Plot of $A_1(r_0)$ vs r_0/R. (b) Plot of $B_1(r_0)$ vs r_0/R. The solid line is obtained from the analytical solution for ψ produced by an infinite-length line charge.

$$\bar{\psi}(r_0) = \bar{\psi}_\infty(r_0) + \delta\frac{\lambda_0}{4\pi^2\epsilon_0 L}A_1(r_0), \tag{34}$$

where

$$\bar{\psi}_\infty(r_0) = \delta\frac{\lambda_0}{8\pi^2\epsilon_0 R}B_1(r_0). \tag{35}$$

Finally, using the results and techniques of Sec. VII A, the contribution from the ends can be written

$$\bar{\psi}(r_0) = \frac{2\delta}{L}\frac{E_{tot}}{q}\tilde{F}(r_0), \tag{36}$$

where

$$\tilde{F}(r_0) = \frac{\tilde{F}_1(k_0R)}{\tilde{F}_2(k_0R)}\frac{\tilde{F}_2(k_0r_0)}{\tilde{F}_0(k_0r_0}, \tag{37}$$

$\tilde{F}_2(k_m r) = J_1(k_m r)Y_1(k_m a) - J_1(k_m a)Y_1(k_m r)$, and the other quantities are as previously defined. For reference, $\tilde{F}(r_0)$ is plotted vs r_0/R in Fig. 9. The total axially averaged asymmetric potential is then

$$\bar{\psi}(r_0) = \frac{\delta}{R}\left\{\frac{\phi_{cw}}{\ln(R/a)}\frac{r_0}{R}\frac{1-a^2/r_0^2}{1-a^2/R^2} + \frac{\lambda_0}{2\pi\epsilon_0}\left[\frac{B_1(r_0)}{4\pi} + \frac{RA_1(r_0)}{L}\frac{}{2\pi} + \frac{2R}{L}J(r_0)\tilde{F}(r_0)\right] + \frac{2R}{L}\frac{kT}{q}\tilde{F}(r_0)\right\}. \tag{38}$$

We see that the asymmetric potential has contributions from five sources. Going from left to right, they are (1) the center wire potential, (2) the electron column and its image charges in an infinite-length model, (3) the finite-length corrections to this model, and (4) and (5) the confining potentials. The relative size of these terms for some experimental data is given in Table III.

VIII. CONCLUSIONS

The diocotron mode has been experimentally studied in a coaxial Malmberg–Penning trap and found to agree with a theory that includes corrections due to a finite-length column and contributions from the confining potentials. When experimental parameters are adjusted to give a very low diocotron frequency, the column orbit abruptly changes to a banana-shaped motion, indicating the presence of a previously undetected field asymmetry in the trap. Modeling shows that a small radial offset in the position of the center wire can account for such an asymmetry.

AUTHOR DECLARATIONS

Conflict of Interest

The author has no conflicts to disclose.

Author Contributions

Dennis L. Eggleston: Formal analysis (lead); Investigation (lead); Methodology (lead); Project administration (lead); Visualization (lead); Writing – original draft (lead); Writing – review and editing (lead).

DATA AVAILABILITY

The data that support the findings of this study are available from the corresponding author upon reasonable request.

APPENDIX A: FINDING THE LINE CHARGE DENSITY λ IN A COAXIAL TRAP

It is a common technique in Malmberg–Penning traps to obtain the line density of the plasma column by measuring the charge on one of the trap rings when the plasma is injected or dumped.[22] The electric field of the plasma column produces a surface charge on the inner wall of the ring that, in total, is equal but opposite the charge on the total capacitance C_r between the ring and ground. C_r includes any discrete capacitance to ground included in the measurement circuit as well as any stray or distributed capacitance (e.g., cable capacitance). Measuring the voltage V_r on this capacitance, thus, results in a measurement of the total charge on the wall of the ring, since $Q = C_r V_r$, and, by Gauss's Law, this is equal in magnitude to the charge of the plasma column

within the ring. This assumes that measurements are made on a timescale short compared to $R_{in}C_r$, where R_{in} is the input resistance of the device measuring V_r.

In a coaxial trap, however, this technique is more complicated because both the center wire and the column produce an electric field at the wall and there are surface charges on both the ring and the center wire.[23] The result is that ring voltage depends not only on the line density λ but also on the position r_0 of the electron column as well as the center wire potential. For example, when the plasma column is long compared to the ring length L_s, we can use

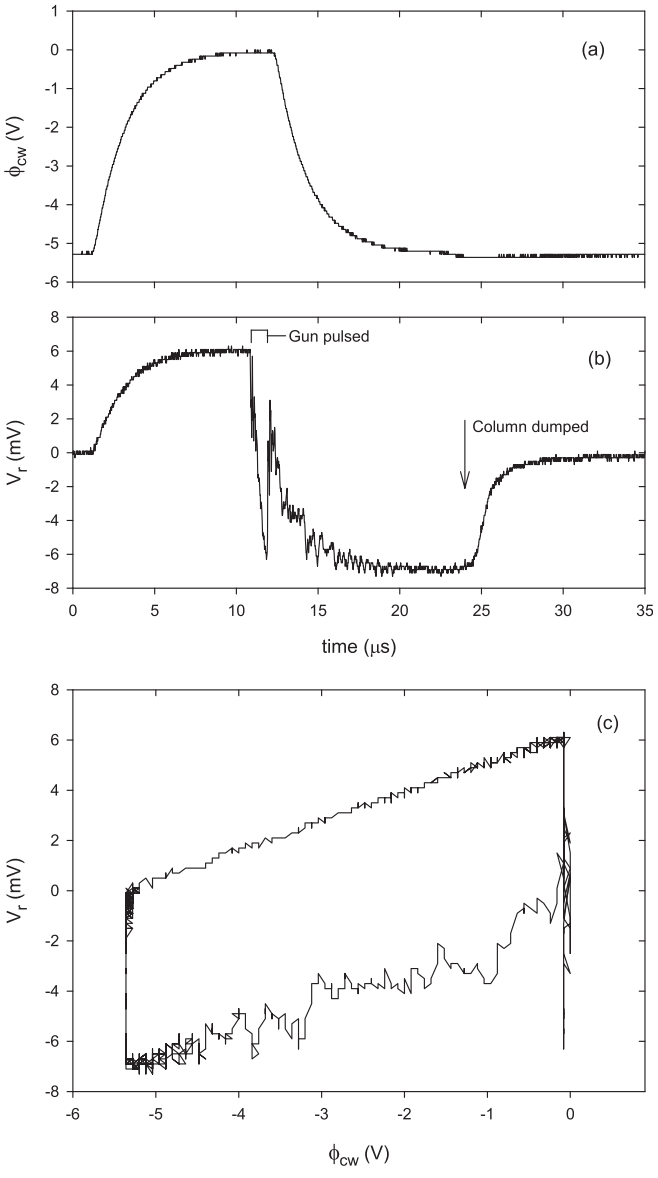

FIG. 11. Typical ring analyzer data showing ϕ_{cw} and V_r vs time in plots (a) and (b), respectively. Electron gun was pulsed at $t = 11\ \mu$s for 1 μs and electrons were dumped at $t = 24\ \mu$s, as indicated. Plot (c) shows the same data plotted as V_r vs ϕ_{cw}.

Eq. (22) for the column potential. Combining this with the center wire potential [Eq. (1)] and taking the radial derivative to obtain the electric field, we can find the surface charge density $\sigma = -\epsilon_0 E_r(R, \theta)$ on the inner wall of the ring. Integrating over the surface of the ring gives the total charge Q. The voltage on the capacitor is then

$$V_r = \frac{Q}{C_r} = \frac{2\pi\epsilon_0 L_s}{C_r \ln(R/a)}\left[\phi_{cw} + \frac{\lambda}{2\pi\epsilon_0}\ln(r_0/a)\right]. \quad \text{(A1)}$$

This should be compared to the simpler expression for a non-coaxial trap: $V_r = \lambda L_s/C_r$. Note that in Eqs. (1) and (22) the wall potential is at ground rather than V_r, so our result assumes V_r is negligible compared to ϕ_{cw} and $\frac{\lambda}{2\pi\epsilon_0}$. This requires C_r to be large compared to the capacitance $\frac{2\pi\epsilon_0 L_s}{\ln(R/a)}$ between the center wire and the wall. These conditions are satisfied in our experiment.

Typical data for this case are shown in Fig. 11, with part (a) showing ϕ_{cw} vs time and part (b) showing the ring voltage V_r vs time. At the start of an experimental cycle, ϕ_{cw} is switched to zero and the electron gun is pulsed. For this example, the electron column is dumped shortly after injection. The V_r signal reflects all of these events.

It is useful to replot these data as V_r vs ϕ_{cw}, as shown in Fig. 11(c). The linear variation in V_r on the top portion of the curve is produced by the variation in ϕ_{cw} before the electrons are injected. The slope of this portion of the curve can then be related to the effective capacitance C_r since the physical dimensions L_s, R, and a are all known. This technique, thus, eliminates the need for a capacitance bridge or other such device to obtain C_r. Also, since the capacitance is obtained from the data itself, there is no question about measuring C_r at the wrong frequency.

The lower half of the curve is produced after the electrons are injected. A linear fit to these data is made with the slope constrained to be the same as the upper curve and the average offset between the two curves obtained. If the column position r_0 is known, this offset is easily related to the line density λ using Eq. (A1).

REFERENCES

[1]For a sampling of current work, see the papers in *Non-Neutral Plasma Physics X*, edited by Matthew R. Stoneking (American Institute of Physics, Melville, NY, 2018).

[2]For other examples of work using a coaxial configuration, see G. Rosenthal, G. Dimonte, and A. Y. Wong, Phys. Fluids **30**, 3257 (1987); S. Robertson and B Walsh, Rev. Sci. Instrum. **70**, 2993 (1999).

[3]D. L. Eggleston, Phys. Plasmas **1**, 3850 (1994); Erratum: **2**, 1019 (1995).

[4]D. L. Eggleston and B. Carrillo, Phys. Plasmas **10**, 1308–1314 (2003).

[5]D. L. Eggleston, Phys. Plasmas **17**, 042304 (2010).

[6]It can be argued that this should be called the magnetron mode[7] since its frequency depends on externally applied electric fields, whereas diocotron modes depend on electric fields from image charges. In practice, such a clean distinction does not hold since our mode frequency depends on electric fields from both sources. Given this ambiguity, we choose the name diocotron mode. We note that this nomenclature is consistent with some previous usage in cases where the electric field producing the motion has contributions from more than one source.[8–10]

[7]See, for example, L. S. Brown and G. Gabrielse, Rev. Mod. Phys. **58**, 233 (1986).

[8]K. S. Fine and C. F. Driscoll, Phys. Plasmas **5**, 601–607 (1998).

[9]J. Fajans, E. Gilson, and E. Yu Backhaus, Phys. Plasmas **7**, 3929 (2000).
[10]E. Sarid, E. P. Gilson, and J. Fajans, Phys. Rev. Lett. **89**, 105002 (2002).
[11]Near-zero frequency diocotron modes and azimuthally restricted orbits were previously observed in experiments with large applied wall voltages (see Ref. 9).
[12]C. F. Driscoll, K. S. Fine, and J. H. Malmberg, Phys. Fluids **29**, 2015 (1986).
[13]D. L. Eggleston, Phys. Plasmas **4**, 1196–1200 (1997).
[14]J. S. DeGrassie and J. H. Malmberg, Phys. Fluids **23**, 63 (1980).
[15]L. Lachhvani, S. Pahari, S. Sengupta, Y. G. Yeole, M. Bajpai, and P. K. Chattopadhyay, Phys. Plasmas **24**, 102132 (2017).
[16]R. N. Bracewell, *The Fourier Transform and Its Applications*, 2nd ed. (McGraw-Hill, New York, 1978), p. 394.
[17]M. Abramowitz and I. A. Stegun, *Handbook of Mathematical Functions With Formulas, Graphs, and Mathematical Tables* (Dover, New York, 1972), pp. 374–376.
[18]Wolfram Research, Inc., *Mathematica, Version 12.0* (Wolfram Research, Inc., Champaign, IL, 2019).
[19]J. D. Jackson, *Classical Electrodynamics*, 2nd ed. (Wiley, New York, 1975), pp. 117–118.
[20]W. R. Smythe, *Static and Dynamic Electricity*, 3rd ed. (McGraw-Hill, New York, 1968), pp. 65–66.
[21]D. L. Eggleston and D. F. Schroeter, Am. J. Phys. **78**, 287 (2010).
[22]J. H. Malmberg and J. S. DeGrassie, Phys. Rev. Lett. **35**, 577 (1975).
[23]An analogous situation occurs on the inner and outer walls of a toroidal trap of rectangular cross section (see Ref. 15).